Bacterial nanocellulose enables auxetic supporting implants

Ajdary, Rubina

2022-05-15

Bacterial nanocellulose enables auxetic supporting implants

Rubina Ajdary [a,e], Roozbeh Abidnejad [a], Janika Lehtonen [a], Jani Kuula [b], Eija Raussi-Lehto [b,c], Esko Kankuri [d], Blaise Tardy [a], Orlando J. Rojas [a,e,*]

[a] Department of Bioproducts and Biosystems, School of Chemical Engineering, Aalto University, P.O. Box 16300, FI-00076 Aalto, Espoo, Finland
[b] Department of Neuroscience and Biomedical Engineering, School of Science, Aalto University, P.O. Box 16300, FI-00076 Aalto, Espoo, Finland
[c] R&D Development Services, Metropolia University of Applied Sciences, PL 4000, 00079 Metropolia, Helsinki, Finland
[d] Department of Pharmacology, Faculty of Medicine, University of Helsinki, 00290 Helsinki, Finland
[e] Bioproducts Institute, Department of Chemical & Biological Engineering, Department of Chemistry and Department of Wood Science, The University of British Columbia, 2360 East Mall, Vancouver, BC V6T 1Z3, Canada

ARTICLE INFO

ABSTRACT

Owing to its purity and exceptional mechanical performance, bacterial nanocellulose (BNC) is well suited for tissue engineering applications. BNC assembles as a network that features similarities with the extracellular matrix (ECM) while exhibiting excellent integrity in the wet state, suitable for suturing and sterilization. The development of complex 3D forms is shown by taking advantage of the aerobic process involved in the biogenesis of BNC at the air/culture medium interphase. Hence, solid supports are used to guide the formation of BNC biofilms that easily form auxetic structures. Such biomaterials are demonstrated as implantable meshes with prescribed opening size and infill density. The measured mechanical strength is easily adjustable (48–456 MPa tensile strength) while ensuring shape stability (>87% shape retention after 100 burst loading/unloading cycles). We further study the cytotoxicity, monocyte/macrophage pro-inflammatory activation, and phenotype to demonstrate the prospective use of BNC as supportive implants with long-term comfort and minimal biomaterial fatigue.

1. Introduction

In addition to plants and trees, cellulose can be biosynthesized by algae (*Valonia*) and some bacteria strains, such as *Komagataeibacter, Sarina*, and *Agrobacterium* (Ross, Mayer, & Benziman, 1991). Cellulose produced by different resources shares the same molecular formula. However, they are used for different purposes, considering their structural and morphological differences. For instance, bacteria-derived cellulose is highly pure and is produced at remarkably high rates and low energy (Gorgieva & Trček, 2019; Naomi, Idrus, & Fauzi, 2020). In addition to purity, bacterial nanocellulose (BNC) has outstanding tensile strength, resulting from nanofibrillar entanglement and the web-like networks it forms. Compared to plant-based cellulose, BNC has a higher degree of polymerization, crystallinity, and water holding capacity. The high porosity of BNC networks, combined with their high surface area, afford materials that display strong interactions with active compounds and therapeutics (Ajdary, Tardy, Mattos, Bai, & Rojas, 2020). Given its biocompatibility (Helenius et al., 2006), BNC is used in

tissue engineering (bone (Cañas-Gutiérrez, Martinez-Correa, Suárez-Avendaño, Arboleda-Toro, & Castro-Herazo, 2020; Oliveira Barud et al., 2020; Pang et al., 2020), skin (Fonseca et al., 2021; Pang et al., 2020), conduits and vascular grafts (Bao, Tang, Hong, Lu, & Chen, 2020; Lee & Park, 2017), drug delivery (Fey et al., 2020), and wound dressings (Anton-Sales et al., 2020; Naomi et al., 2020; Queirós et al., 2021)). In addition to biomedical applications, BNC has been studied as a platform for immobilization (Cai et al., 2018; Yuan, Chen, Hong, & Zhu, 2018), and membrane filtration (Lehtonen et al., 2021; Xu et al., 2018).

Various methods have been used for BNC production, including static and agitated culturing in bioreactors. The static method was followed in this research and involved the formation of gelatinous membranes (biofilms) on the surface of a support that provided access to oxygen (aerotaxis) and nutrition from the culture medium. The bacteria strain and culture conditions (pH, nutrition, oxygen delivery, temperature) have a determining impact on BNC's properties. *Komagataeibacter*, also known as *G. xylinum*, has a higher BNC production rate than other bacteria types (Wang, Tavakoli, & Tang, 2019). Such non-

photosynthetic, aerobic bacteria strain converts glucose and other organic compounds into cellulose within a few days. Despite BNC's inherent characteristics, most of the material developments have focused on full-infill planar structures and obtaining precise geometries. Recently, Greca et al. (Greca et al., 2020; Greca, Lehtonen, Tardy, Guo, & Rojas, 2018) proposed a facile and customizable approach to fine-tune the morphology of BNC, in all directions of (x, y, z), by super-hydrophobization of the solid support, and altering the hydrostatic pressure and accessibility to nutrients. Rühs et al. (2020) developed a universal method to grow a BNC coating *in situ* on the external surface of complex 3D objects. The BNC demonstrated enhanced lubrication and functioned as a load-bearing network with high energy dissipation under shear and compression.

Molding and silicone templating allow the development of customized structures. However, the latter have not evolved further since their introduction, more than three decades ago (Bungay & Serafica, 1986). Bottan et al. (2015) investigated molding techniques for bio-lithography guided-assembly and introduced texture on BNC surfaces. Geisel et al. (2016) developed a process to guide the neural stem cells through controlling the surface topography of BNC and by growing it on patterned multi-level polydimethylsiloxane (PDMS) substrates. Yang et al. (Yang et al., 2018) applied micropatterning in PDMS to manufacture bacterial cellulose-based intervertebral disc implants that demonstrated excellent tissue integration and shape stability (at least 3 months after implantation in rats).

Herein, we produced BNC structures with superior structural integrity and auxetic behavior, as defined by the Poisson's ratio, the relative change in the natural dimension under directional load (Lakes, 2017). The term *auxetic* refers to materials with negative Poisson's ratio, which counterintuitively expand in a direction normal to that of the tension or load (Knight, Moalli, & Abramowitch, 2018; Papadopoulou, Laucks, & Tibbits, 2017; Prawoto, 2012). While auxetic assemblies are rare in nature, they are found in iron pyrites, pyrolytic graphite, cadmium, zeolite, and in some tissues (cat skin, cancellous bone) (Lakes, 1987; Liu & Hu, 2010). Remarkable auxetic geometries have been studied for biomimicry to develop a wide range of materials, for example, by using additive manufacturing (Cheng et al., 2020; Jiang & Li, 2018). According to molecular mechanics, crystalline cellulose I$_\beta$ demonstrates an auxetic effect by unfolding the crystalline chains along the loading direction (Yao, Alderson, & Alderson, 2016). On a larger scale, some commonly used cellulosic papers exhibit auxetic response depending on the structure of the fiber network and processing conditions, which impact the interwoven fiber organizations and hydrogen bonds at junction points (Verma, Shofner, & Griffin, 2014).

Synthetic plastic meshes (those made with polypropylene or PP) are commonly implanted in the body to treat gynecological pelvic disorders and hernias in clinical practices. The implanted structures support, lift, or hold any weakened tissue in the desired position. Although PP implants have been applied in clinical practice since 1958 (Baylón et al., 2017), overall statistics reveal the challenges associated with the remarkable chemo-mechanical downgrade after implantation, suggesting that the implanted PP used for surgical treatments is not inert in the human body (Ajdary et al., 2021; Iakovlev, Guelcher, & Bendavid, 2015; Sternschuss, Ostergard, & Patel, 2012). According to the literature, PP undergoes various degrees of degradation (*e.g.,* oxidative degradation, depolymerization, additive leaching), stress cracking, shrinkage, and cause infection and inflammation (Sternschuss et al., 2012). The disadvantageous associations and patient-reported complications were reasons for the U.S. Food and Drug Administration to ban some PP mesh products available in the market in 2019 (U.S. Food and Drug Administration, 2021).

Controlling structural changes under load is an essential feature in biomedical structures. The openings in mesh implants are often designed and reported under no loading. However, when implanted, the opening geometry considerably changes according to the applied load. For example, the void openings of polypropylene meshes, used as a typical implant material, are easily collapsed under load (for example, in the pelvic floor). Unfortunately, the shrinkage of the void openings (<1 mm) challenges tissue ingrowth and possibly leads to inflammation, pain, and an increased risk of bridging fibrosis (Knight et al., 2018). Previous reports emphasize the importance of maintaining the void openings to better integrate the structure with the host tissue and minimize the challenges caused by geometrical changes in the structure. Auxetic structures could be designed to facilitate larger openings that efficiently and geometrically comply with the anatomical changes during movements and dynamic deformations (Stavric & Wiltsche, 2019).

As described herein, the combination of additive manufacturing and mold templating techniques enabled the formation of auxetic BNC structures for biomedical uses and with controlled structural patterns, openings, and mechanical performance. BNC, with high similarity to the extracellular matrix, excellent porosity (from mesoporous to macroporous range), and exceptional wet strength, is a promising alternative to replace PP meshes.

2. Experimental section

2.1. Materials

The strain used for BNC production (*Komagataeibacter medellinensis*) was supplied by the School of Engineering, Universidad Pontificia Bolivariana, Colombia (Castro et al., 2013). D-(+)-Glucose, yeast extract, peptone, sodium phosphate dibasic, and citric acid were purchased from Sigma Aldrich (St. Louis, MO, USA). Phosphate buffer saline (pH 7.4) and acetate buffer solution (pH 5) were used in the characterizations. Milli-Q water (purified with a Millipore Synergy UV unit, Burlington, MA, USA) was used throughout the experiments (18.2 MΩ cm). Other solvents included ethanol (ETAX Aa 99.5%, Aldrich, Steinheim, Germany) and acetone (AnalaR NORMAPUR 99.8%, VWR Chemicals). GYNECARE TVT EXACT® polypropylene mesh was purchased from Johnson & Johnson (New Brunswick, NJ, USA) and was utilized as a control sample for *in vitro* tests. The THP-1 human monocyte/macrophage cell line was obtained from the European Collection of Authenticated Cell Cultures (ECACC, cat#88081201, Salisbury, UK).

2.2. Design and fabrication of auxetic molds

Three auxetic 3D models (triangle, round, star) were designed by using Solidworks, and the files (STL format) were sliced by an Ultimaker Cura software. The polylactic acid filament was processed by additive manufacturing using Fused Filament Fabrication (Ultimaker 2) to 3D print triangle, round, and star molds (10 cm × 10 cm × 4 cm), used as positive molds. Then, Mold Star TM 30 silicone rubber (components A and B) was used to fabricate the respective negative molds. Firstly, an equal mass ratio of component A and part B were added together and mixed. Then, the 3D printed models were placed in a square-shaped container, and the mixed silicone rubber filled the 3D printed models and the container. The full curing time of the silicone rubber was about 6 h. However, partial hardening was initiated after about 30 min after mixing the components A and B. After full curing in room condition, the 3D printed models were taken out, yielding soft silicone molds. The steps used in preparing the silicone molds from the 3D models are displayed in Fig. 1.

2.3. Synthesis of BNC structures

First, glucose, yeast extract, peptone, and Na$_2$HPO$_4$ were mixed using a dry mass ratio of (8:2:2:1). Then MilliQ-water was added (1 L final volume containing 20 g glucose, 5 g yeast extract, 5 g of peptone, 2.5 g of Na$_2$HPO$_4$). All the components were dissolved, and the pH of the medium was adjusted to 4.5 with citric acid. The container was then sterilized in an autoclave for 15 min at 121 °C, then cooled to room temperature. Later, the bacterial strain was added to the bottle and was
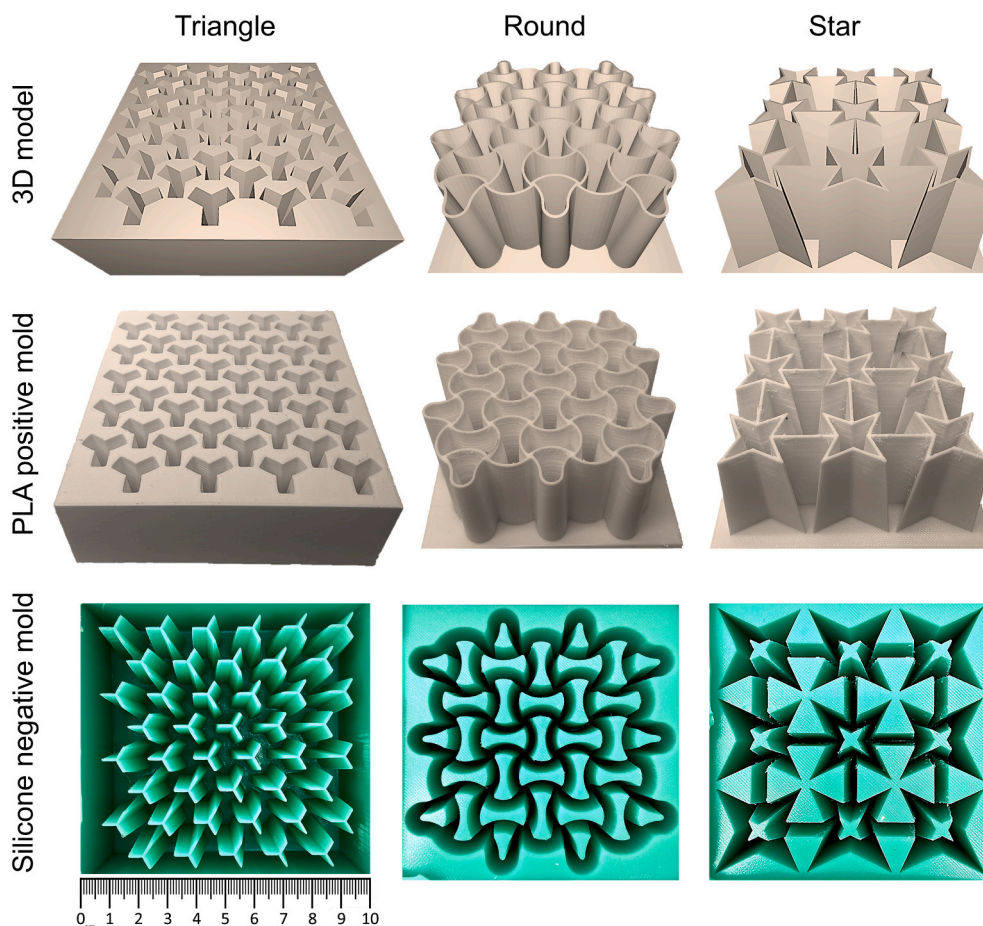
Fig. 1. From auxetic 3D-printed models to cast silicone molds. From left to right, triangle, round, and star auxetic shapes. Top — 3D models. Middle — 3D printed molds produced by fused filament fabrication of PLA filaments. Bottom — cast silicone auxetic molds.

shaken gently to distribute it homogeneously. Then, the BNC culture medium containing the bacteria was poured into the sterilized silicone molds (previously autoclaved at 121 °C, 1 bar), covered, and sealed with parafilm. The medium was left still for 7 to 14 days at 28 °C in the incubator. After the given time, the produced bacterial cellulose biofilm was washed several times with deionized water and left in deionized water for one day. The water was changed several times within the day to remove the components used in the growing medium. Then, the bacterial cellulose pellicle was purified with 0.1 M NaOH at 60 °C for 4 h and, thereafter, washed several times in hot deionized water (6 h).

2.4. Characterization of mold-guided auxetic BNC structures

2.4.1. Surface area
The surface area and the average pore size of freeze-dried BNC were measured by N_2 adsorption at given relative pressures (Micromeritics Tristar II), following the Brunauer–Emmett–Teller (BET) and Barrett–Joyner–Halenda (BJH) models. Before the measurements, the BNC samples were frozen at −18 °C, followed by freeze-drying under vacuum (−49 °C for at least 48 h). Prior to BET analysis, a degassing step was performed for 4 h at 120 °C.

2.4.2. Structure
A Java-based image analysis program, ImageJ, was used to determine the size of the openings and the overall structural infill density (Rueden et al., 2017). The microstructure of the surface and cross-section of BNC was observed with a Zeiss Sigma VP scanning electron microscope (Carl Zeiss AG, Oberkochen, Germany) operated at an accelerated voltage of 2 kV. Prior to imaging, the samples were fixed on

a metal stub using double-sided carbon tape and sputtered with a 3–4 nm layer of gold-palladium alloy using a LEICA EM ACE600 (Leica Camera AG, Wetzlar, Germany) sputter coater.

2.4.3. Weight loss
The dried samples were cut into pieces of similar size (using an 8-mm round biopsy punch) and weighted (W_0) separately. Then, the samples were immersed in 3 ml buffer (acetate buffer solution, pH 5) and phosphate buffer saline (PBS, pH 7.4) for 28 days at 37 °C. At each time point (1, 7, 14, 21, 28 days), the samples were taken from the buffer, washed with deionized water, re-dried at 37 °C for 24 h, and weighed again in the dry state (W_d). Finally, the weight loss was calculated using the equation below.

$$\text{Weight loss } (\%) = \frac{W_0 - W_d}{W_0} \times 100.$$

2.4.4. Mechanical properties
Ball burst strength or burst resistance of the wet BNC films was measured with a TA.XTP*lus* Texture Analyzer (Stable Micro Systems Ltd., Surrey, UK) equipped with a spherical SMS P/0.25S probe. To perform the test, a BNC film (disc-shaped, 5-cm diameter) was placed and fixed between two discs containing a 1-cm diameter opening in their centers. Sandpaper was attached to the internal section of the discs to avoid slippage of the BNC films (Fig. S1). An Exponent Connect software was used to analyze the data after the measurement. To determine the performance stability, measurements were repeated during 100 cycles at 3% strain and at a 120 mm/min measurement speed.

The tensile measurements of wet BNC ribbons were conducted by

using TA.XTP*lus* Texture Analyzer (Stable Micro Systems Ltd., Surrey, UK) equipped with a miniature tensile grip. The BNC specimens tested (cross-head speed of 5 mm/min) had a gauge length of 2.5 cm (S. Wang et al., 2018), and a thickness varying from 0.8 mm to 2.7 mm (measured by a digital caliper after a culturing time of 7, 10, 14 days). The texture in the internal section of the grip inhibited the slippage of the BNC ribbon (Fig. S2).

The Poisson's ratio of the BNC structure was calculated by analyzing a recorded video of the structure under manual stretching through MATLAB 9.7 R2019b (MathWorks Inc., Natick, MA, USA) image processing toolbox. The images extracted from the videos were further analyzed by ImageJ software to determine the transverse and the longitudinal strains. Finally, Poisson's ratio was calculated following the equation below at a single strain value (Lai & Yu, 2020).

$$Poisson's \ ratio = -\frac{Transverse \ strain \ (\varepsilon_T)}{Longitudinal \ strain \ (\varepsilon_L)}.$$

2.4.5. Cell culturing and incubation

The human monocyte/macrophage cell line, THP-1, was cultured in Roswell Park Memorial Institute (RPMI)-1640 medium (GiBNCo 31870-025, Thermo Fisher Scientific, Waltham, MA, USA) supplemented with 10% heat-inactivated fetal bovine serum (GiBNCo 10500-064), 2 mM ʟ-glutamine (GiBNCo A2916801) and antibiotics (GiBNCo 15140-122, penicillin G 100 U/ml, streptomycin 100 μg/ml and GiBNCo 15290-026, amphotericin B 250 ng/ml) under regular cell culture conditions (+37 °C humidified atmosphere supplemented with 5% CO_2). Before experimentation, the materials were incubated overnight in 70% ethanol and washed meticulously with phosphate-buffered saline without calcium or magnesium (Lonza Bio Whittaker, 17-516F, Basel, Switzerland), followed by washes in a culture medium. At the beginning of the experiments, a 6-mm diameter biopsy punch (BP-60F, kai Europe GmbH, Solingen, Germany) was used to cut round, equal-size samples of the materials that were placed individually into wells of a non-adherent 96-well plate. THP-1 cells were counted using an automated cell counter (Countess II, Applied Biosystems, Thermo Fisher Scientific), and 80,000 cells/well suspended in culture medium were pipetted to each well with material as well as to the empty control wells without material. 12-O-Tetradecanoylphorbol-13-acetate (TPA, Sigma P8139, Merck KGaA, Darmstadt, Germany) at a final concentration of 300 nM was used to induce macrophage differentiation of the THP-1 cells, as reported previously (Väänänen, Salmenperä, Hukkanen, Rauhala, & Kankuri, 2006).

2.4.6. Microscopy

Phase-contrast microscopy of THP-1 cells incubated with or without the materials was carried out using an Olympus CKX-41 inverted microscope and 20× objective (Olympus Corporation, Tokyo, Japan). Black and white images of cell morphology on the bottom of the wells were obtained using a digital microscope camera (DC 300, Leica Microsystems GmbH, Wetzlar, Germany) fitted with a 0.5× adapter (U-TV0.5XC-3; Olympus). Leica IM 500 software (version 1.20 release 19, Leica Microsystems) was used for image documentation.

2.4.7. Measurements of cytotoxicity and pro-inflammatory cell activation

After a 3-day incubation of undifferentiated or TPA-differentiated THP-1 monocyte/macrophages with or without the materials, the culture medium was collected for analysis. Immediately after collection, the samples were centrifuged at 20,000 rpm for 10 min to remove any cell debris or particulates; supernatants were divided into aliquots and transferred to new tubes for storage at −20 °C until analysis. Cytotoxicity was measured from the culture medium supernatant using the colorimetric LDH cytotoxicity detection kit plus (Roche 04744926001, Merck) according to the manufacturer's instructions and as described earlier (Den Hollander et al., 2015). Briefly, 100 μl of the assay reagent was mixed with 100 μl of the cell culture sample supernatant. After a 30-min incubation in the dark at room temperature, the reaction was

stopped, and spectrophotometric analysis was performed using a microplate reader. The optical density results at 492 nm were corrected with those at 620 nm. Levels of basal LDH activity measured from naïve culture medium samples were subtracted from the obtained values prior to analysis.

Concentrations of interleukin-8 (IL-8) in the supernatant of the culture medium samples were measured using a human IL-8 specific enzyme-linked immunosorbent quantitative assay (ELISA, 88-8086; Invitrogen, Thermo Fisher Scientific) according to the manufacturer's instructions. If needed at re-analysis, samples initially measuring with too high IL-8 concentrations (not within the assay linear range) were pre-diluted in naïve culture medium. Briefly, 96-well ELISA plates (NUNC maxisorp, 442404, Thermo Fisher Scientific) were coated with the capture antibody overnight at +4 °C. The wells were aspirated and washed four times with the kit-supplied wash buffer using an automated programmable plate washer (Wallac 1296-026 Delfia Platewash, PerkinElmer Inc., Waltham, MA, USA). Non-specific binding was blocked with assay diluent for 1 h at room temperature, and wells were washed with wash buffer. Samples (100 μl) were then pipetted into the wells, and the plate was incubated for 2 h at RT. After four wash cycles, 100 μl detection antibody was added to each well, incubated for 1 h, and followed by four wash cycles. The Avidin-HRP conjugate was added to the wells, incubated for 30 min, followed by four wash cycles. The tetramethylbenzidine substrate solution was added to each well, the plate was incubated for 15 min, and a stop solution was added to end the reaction. The optical density was measured using a microplate reader at 450 nm wavelength and 570 nm correction wavelength. Naïve culture medium served as a baseline-control sample. Samples for the standard curve were included in each assay run. The standard curves for each assay run were generated using non-linear regression sigmoidal 4-parameter-logistic curve-fitting, and sample concentrations were interpolated from the curves in GraphPad Prism 9 software (version 9.0.1, GraphPad Software LLC, San Diego, CA, USA). Statistical analysis was performed in GraphPad Prism using the nonparametric Mann-Whitney test where *p* values less than 0.05 were considered significant.

3. Result and discussion

3.1. Auxetic designs and culture time

Additive manufacturing techniques, such as fused filament fabrication, allow the production of complex structures challenging and arduous to form with other methods. Still, the slow production rate during fused filament fabrication does not allow the rapid manufacturing of multiple copies. Combining the fused filament fabrication technique and silicone molding accelerated the process to form functional molds for the growth of mechanically robust BNC networks. Three auxetic designs, namely, "triangle", "round", and "star" shapes, were evaluated to demonstrate the fabrication of BNC biomaterials. These designs facilitated the formation of structures of a tunable opening size to fulfill the minimum 1-mm opening width required for biomedical structures. As shown in Fig. 1, all three mold designs were cast with silicone to produce molds with a high level of detail and accuracy. Beyond the three designs evaluated herein, this method offers potential for any planar auxetic designs.

Initially, the positive and negative molds were developed with a tilt angle of 0 degrees between the base of the molds and the templating pillars (Figs. S3, S4). However, according to the experimental observations, a tilt angle of about 5° in the positive 3D model facilitated the silicone molding process (Fig. 2a–b, Fig. S5). Also, compared with the structure developed in the 0-degree molds, the slight tilt angle in the mold simplified the removal of the BNC network, which was obtained after culturing for 7, 10, and 14 days. The tilted angle in the silicone mold may also function as additional support for the BNC network in the air/culture medium interface. Importantly, the total volume of the culture medium in the tilted negative silicone molds impacted the height of
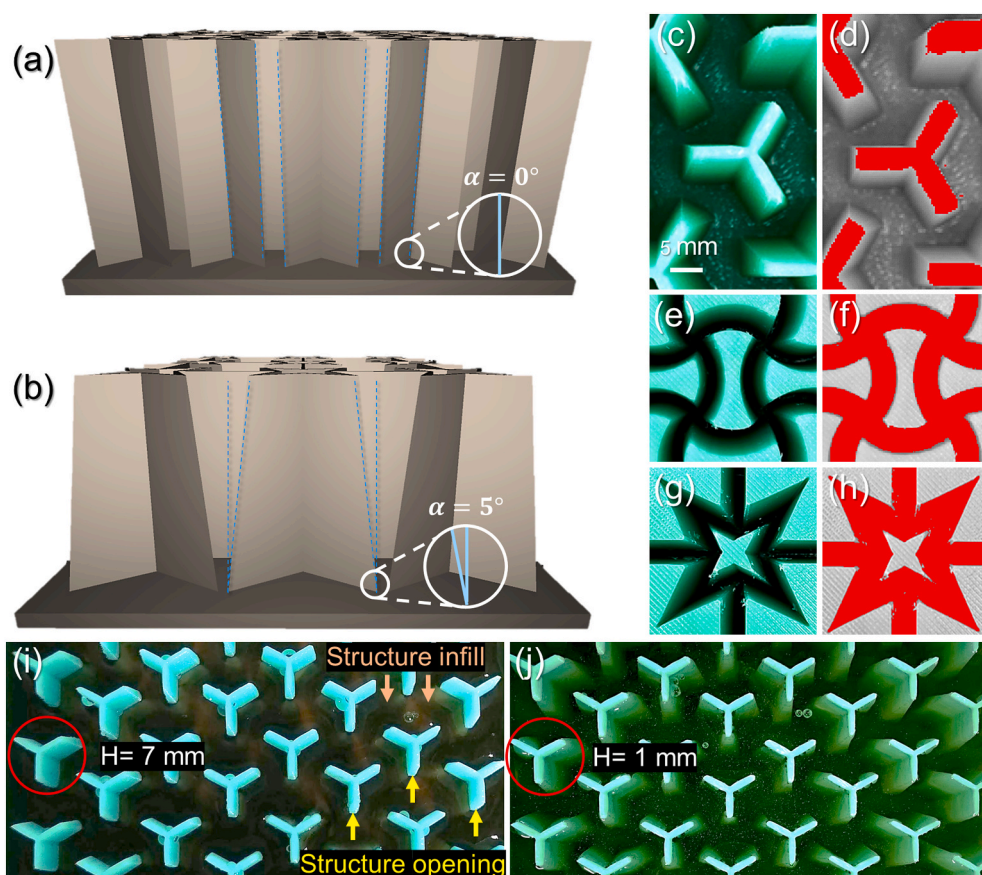
Fig. 2. The tilt angle (a) α = 0 and (b) α = 5° in the positive mold and its impact on the openings of the structures. Due to the angle, α = 5°, the higher the level reached by the BNC culture medium, the larger BNC infill is obtained in the final mesh. (c) The triangle auxetic unit cell and (d) the maximum infill (the smallest opening) obtained under complete filling of the mold with BNC culture medium. (e, f) Round auxetic unit cell, and (g, h) star auxetic unit cell. (i) The triangle mold filled partially, and (j) fully with BNC culture medium.

the BNC structures formed, thus the opening size and the infill density in each design. For instance, the higher structure infill density was associated with smaller openings as the level of culture medium increased in the silicone mold (Fig. S5). The minimum opening size (largest infill density) was obtained when the culture medium completely filled the mold, as indicated in Fig. 2 for each design. Based on the image analysis of the obtained BNC structure, the maximum infill density in the triangle design was 70 ± 3.1% (about 30% openings), while this value was 59 ± 2.1 and 62 ± 2.6% for the round and star shapes, respectively. Note that proper covering and sealing of the culture medium containing molds with parafilm minimized the evaporation of the liquid.

3.2. Characterization of auxetic BNC structures formed by aerotaxis

3.2.1. Mold-guided auxetic BNC materials

Auxetic geometries exhibit exceptional structural properties (e.g., controllable expansion under tension and geometrical compliance to the anatomical changes during movements and dynamic deformation), going beyond their material composition (Stavric & Wiltsche, 2019). Herein, we combined 3D printing and molding techniques to develop mold-guided BNC structures via hybrid manufacturing. The full process, from the 3D model to the final extracted mesh, is shown in Fig. S6. Each of the developed systems demonstrated anisotropic mechanical response and negative Poisson's ratio. The calculated Poisson's ratio deviated according to the auxetic unit (opening shape and size) and the extent of applied stress, as well as its directionality. Never-dried purified BNC structures cultured for 10 days displayed a negligible change in thickness upon stretching and exhibited auxetic properties, as shown in Figs. 3 and S7. The triangle unit cell had a negative Poisson's ratio of $v = -0.19$, while the value for the round and star auxetic unit cells were $v = -0.36$ and $v = -0.13$. The reversible structural expansion under tension can minimize tissue damage, which commonly occurs during shrinkage

of the plastic-based mesh implants and supports the dynamic and repeated body movements.

3.2.2. Porosity, surface area, and microstructure

The static BNC culturing method resulted in cellulose hydrogel (BNC) membranes that form at the air/culture medium interface. Herein, the bacteria access to air at the interface between the liquid culture medium and the silicon surface, in a process called aerotaxis. The aerobic bacteria strain transforms glucose, and other organic nutrients into cellulose, within a few days. These bacteria, like other living organisms, have an optimum growth environment with controlled factors such as oxygen, temperature, culture time, and pH. The physicochemical properties of BNC structures were highly dependent on the environmental factors, and the variables could be narrowed down to study the BNC formation. Aerobes such as *K. medellinensis*, require oxygen for energy conversion and cellular respiration. These requirements for an optimum growth environment (pH, temperature, oxygen) were met by adjusting the pH to 4.5 and maintaining the static culture in an incubator at 28 °C. As indicated in Fig. 4a, the BNC thickness increased with the culture time since the bacteria had more time to generate and accumulate more nanofibrils. The substantial water content in the hydrophilic BNC slowed down the drying at room conditions. As shown in Fig. S8, it took about 72 h for the structure to lose 95% of the initial water. As the thickness of BNC increased with the culture time, structures with larger BET surface areas were obtained. A BET surface area of about 25 m^2 g^{-1} to almost 60 m^2 g^{-1} resulted from 7 to 14 days of culturing (Fig. 4b, Fig. S9). Importantly, increasing thickness due to increased incubation also resulted in high cross-linking of the network, and thus in smaller mesopores (Fig. 4b), as was also previously inferred from measuring the flow across BNC membranes (Lehtonen et al., 2021). However, the never-dried BNC was expected to have a larger surface area compared with the freeze-dried ones since the hydrophilic BNC
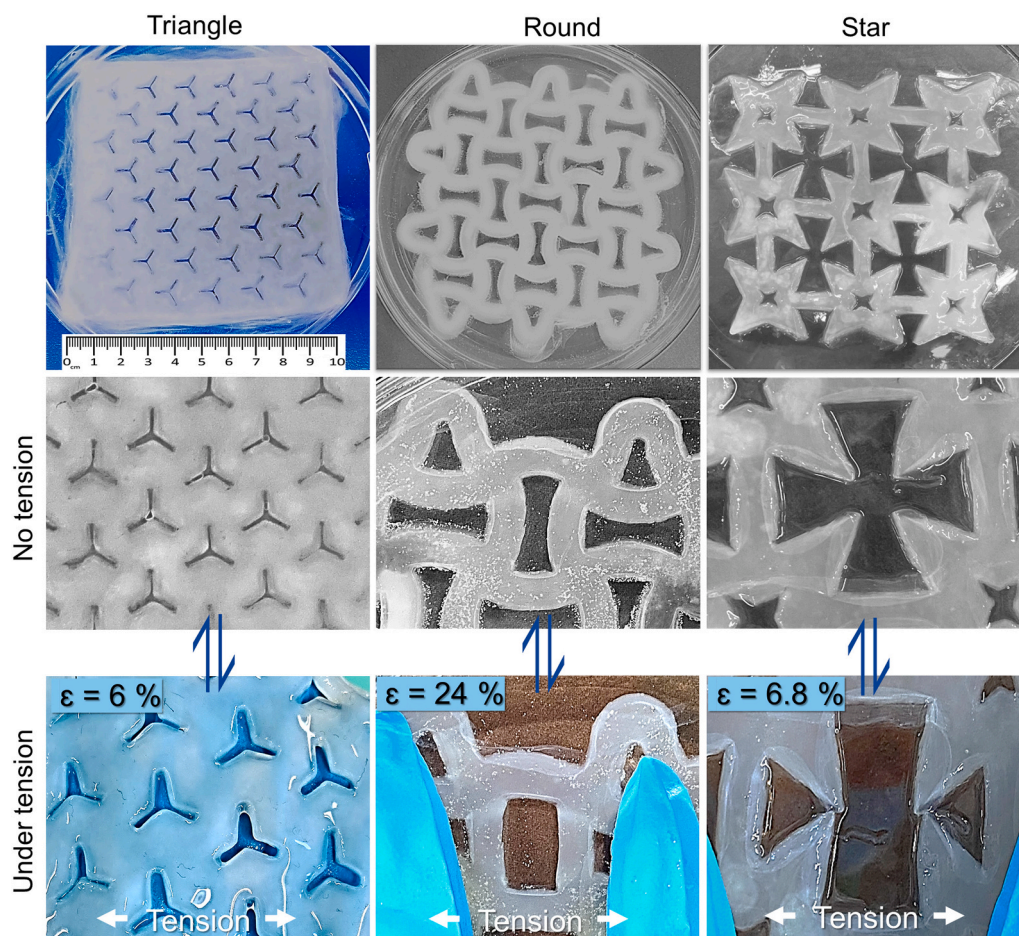
Fig. 3. Auxetic BNC meshes obtained after 10 days of culturing (triangle, round, and star patterns). The structures exhibit reversible expansion under tension.

undergoes irreversible hydrogen bonding when dehydrated for the sample preparation step in BET characterization. The culture time had no evident effect on the surface and cross-section of the microstructures. As shown in Fig. 4, the interfacially grown, physically entangled BNC showed a relatively dense network, while the cross-section of the lyophilized BNC was highly porous (macroporous range and voids, not measured by BET). Although the solid content in the BNC structure was less than 0.5 wt%, the physically entangled nanofibrils retained the porous microstructure after freeze-drying and provided mesoporous structure, ideal for the nutrition and oxygen transport in the wet BNC. As shown in Fig. S10, the *solid* morphology of PP does not provide a microenvironment similar to the ECM, and the interstices between the multi-filaments could host bacteria and immune cells and lead to inflammation and infection in the tissue (Dällenbach, 2015).

3.2.3. Weight loss

The pH during incubation is a critical factor in BNC growth; an acidic environment has been demonstrated to enhance the bacterium activity to produce thicker BNC pellicles. A deeper investigation to assess the importance of pH showed that although more BNC was formed at lower pH (pH 5 to pH 3.5), pellicles were hardly formed at pH 3 and below (Aramwit & Bang, 2014). However, this might vary depending on the BNC strain. In this work, the growing pH was fixed at the beginning at 4.5, for all samples. Additionally, we aimed at studying the BNC weight loss at pH 7.4 (normal body condition) and pH 5 (pH associated with some body parts such as the areas in the pelvis, duodenum, small intestine, and colon) (Fallingborg, 1999; Savchenko, 2021). According to previous degradation studies (Ajdary et al., 2020; Lin & Dufresne, 2014), highly crystalline structure of nanocellulose prevents

degradation, which otherwise would take place through enzymatic activities or a combination of hydrolytic mechanisms and autocatalytic oxidation. The higher degree of polymerization and crystallinity (~90%) of BNC compared with the values for the plant-based nanocellulose (crystallinity of 44–65%) has a substantial effect on the more challenging structural degradation (Amorim et al., 2020). After 28 days of exposure to pH 7.4 and pH 5, the pellicles exhibited mass loss of less than 2% and 4%, respectively, mostly due to the fibrils' detachment when handling the material during the washing step and characterization (Fig. S11). This suggests that the BNC structures are potential candidates to facilitate long-term tissue support.

3.2.4. Mechanical performance

Biomaterials, especially those used to support organs, are expected to be strong, flexible, stable, and biocompatible with the target tissue, *i.e.*, to be able to lift and hold the intended weight when used *in-vivo*. Both burst and tensile strength are viable approaches to examine the pressure retention of materials and implants under load. Our biofabricated BNC meshes exhibited high flexibility due to the large water content (>99.5 wt%) and long aspect ratio of the nanofibrils. The dense physical entanglement of high aspect ratio nanofibrils translated into robust mechanical performance, as shown in Fig. 5. In tensile mode (Fig. 5a), the wet BNC ribbon load-elongation curve resembled that of Achilles tendons (Barfod, 2014), where the toe region occurs at below 1% strain. As the load increased, the crimped nanofibrils straightened until microscopic and macroscopic failure occurred and the BNC ribbon ruptured, after 2–4% elongation, depending on the BNC culture time. The wet BNC structure underwent slightly higher elongation under ball burst testing with the load reaching 15 N (1.53 kg) and 26 N (2.65 kg)
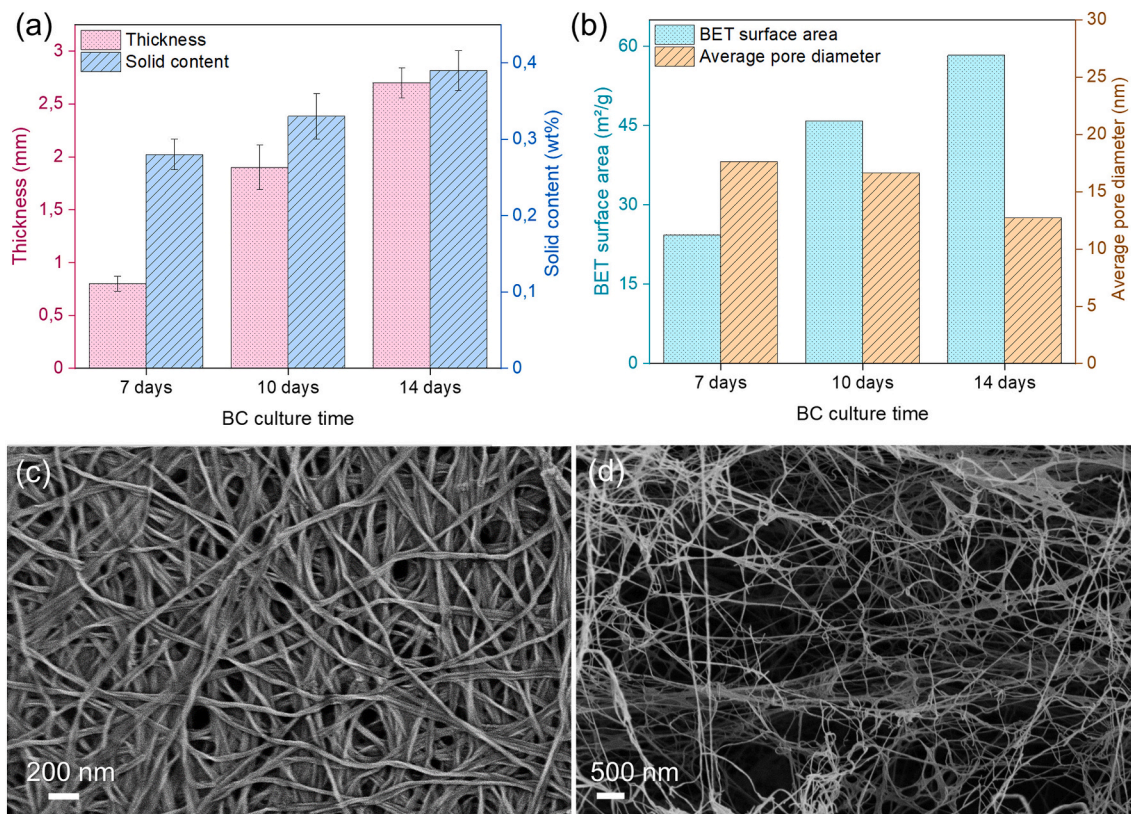
Fig. 4. (a) The BNC structure thickness and solid content produced after 7, 10, and 14 days incubation. (b) The BET surface area and the average pore diameter for BNC samples cultured for 7, 10, 14 days. The SEM images of (c) BNC surface at 30,000× magnification, and (d) BNC cross-section at 10,000× magnification.
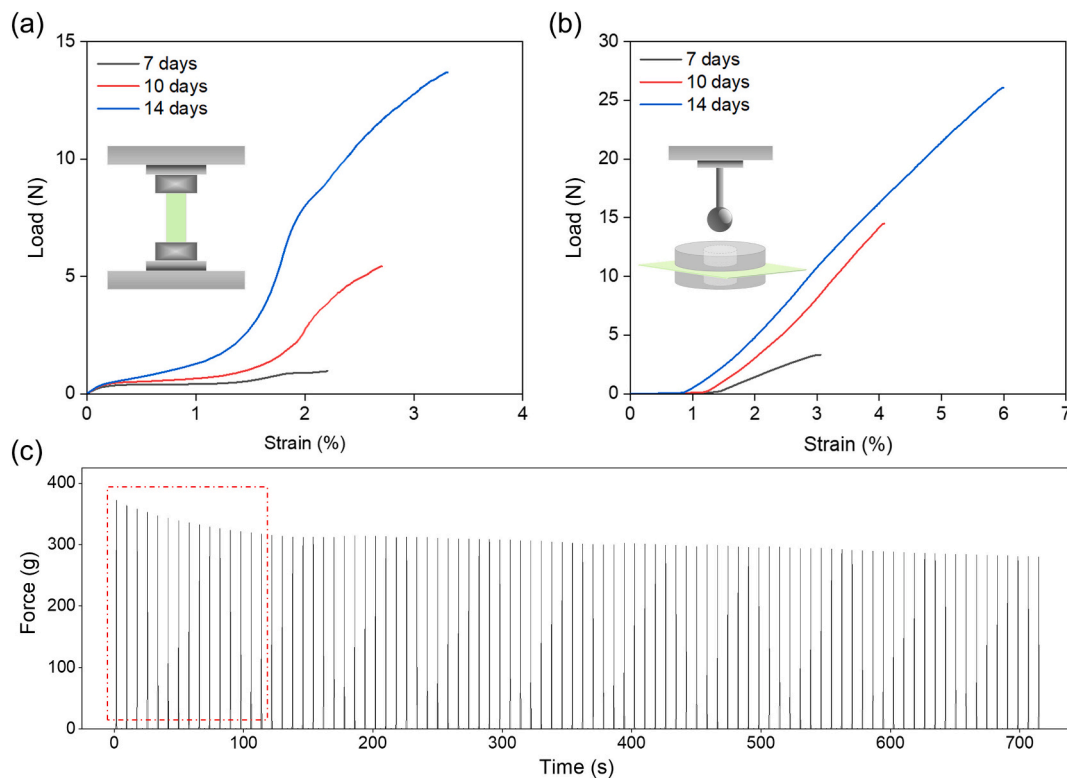

Fig. 5. (a) The load-elongation curve for BNC samples subjected to tensile tests, and (b) load-elongation profiles for BNC ball burst strength tests for BNC samples after 7-, 10-, and 14-days culture time. (c) The cyclic burst strength during 100 cycles at 3% strain.

for BNC samples cultured for 10 and 14 days, respectively, before samples rupture. The mild NaOH purification treatment had a negligible effect on the modulus and tensile strength properties of the BNC. However, some reports demonstrated a decrease in the entanglement density and porosity of the nanofibrils due to the microstructural swelling after strong alkali post-treatments (McKenna, Mikkelsen, Wehr, Gidley, & Menzies, 2009; Tang, Jia, Jia, & Yang, 2010). The values of ultimate tensile strength of wet BNC increased ten-fold, from 48.9 ± 6.3 MPa to 456.2 ± 33 MPa by prolonging the incubation time, from 7 to 14 days, respectively. These values are comparable with that of human muscle tissue (Barnes, Przybyla, & Weaver, 2017), and the exceptionally high water content in BNC provided a lubricious surface that tended to reduce the soft tissue friction during mobility and activity. A purified BNC film (10 days) was studied further to examine the effect of cyclic loading on the performance. While 9% reduction occurred in the first 15 cycles, 87% of the performance was sustained after 100 cyclic loadings (Fig. 5c). Other reports have shown that the exceptional mechanical performance of BNC equips the microstructure with suture retention capabilities, which is an important factor in implants (Hong, Wei, & Chen, 2015).

3.2.5. Cytotoxicity and interleukin-8 release from THP-1 cells

Cellular gross morphology was evaluated after 3-day incubation. The release of lactate dehydrogenase (LDH) from the cells to the culture medium was evaluated as a marker of cell membrane damage and material-induced cytotoxicity, and concentrations of IL-8 were quantified to evaluate monocyte/macrophage pro-inflammatory activation and phenotype (Fig. 6). In undifferentiated THP-1 monocyte cultures, both polypropylene control and BNC demonstrated a cell-flattening effect suggesting minor to moderate differentiation into a macrophage-like phenotype (Fig. 6a–c). Induction of macrophage differentiation using TPA was manifested in all cultures as dominant cell flattening on the non-adherent culture surface (Fig. 6d–f). A shift towards a macrophage-like phenotype was further indicated by the increased release of LDH (Fig. 6g) and an increased secretion of IL-8 from the undifferentiated THP-1 cells incubated with BNC (Fig. 6h). When a dominant macrophage-like phenotype was induced on the THP-1 cells by TPA, a more than 400-fold increase in the release of IL-8 was observed. Incubation of these differentiated cells with BNC suppressed the pro-inflammatory macrophage phenotype as evidenced by a significantly decreased secretion of IL-8 into the culture medium (Fig. 6h). Incubation with BNC also suppressed the THP-1 cells pro-inflammatory macrophage differentiation-associated increase in LDH release (Fig. 6g). Taken together, BNC drove monocyte activation but suppressed the TPA-induced pro-inflammatory macrophage-like phenotype. The observed activities of BNC on human monocyte/macrophages deserve further attention. Further research focusing on the type of macrophage differentiation activated by the BNC can be expected to provide a deeper
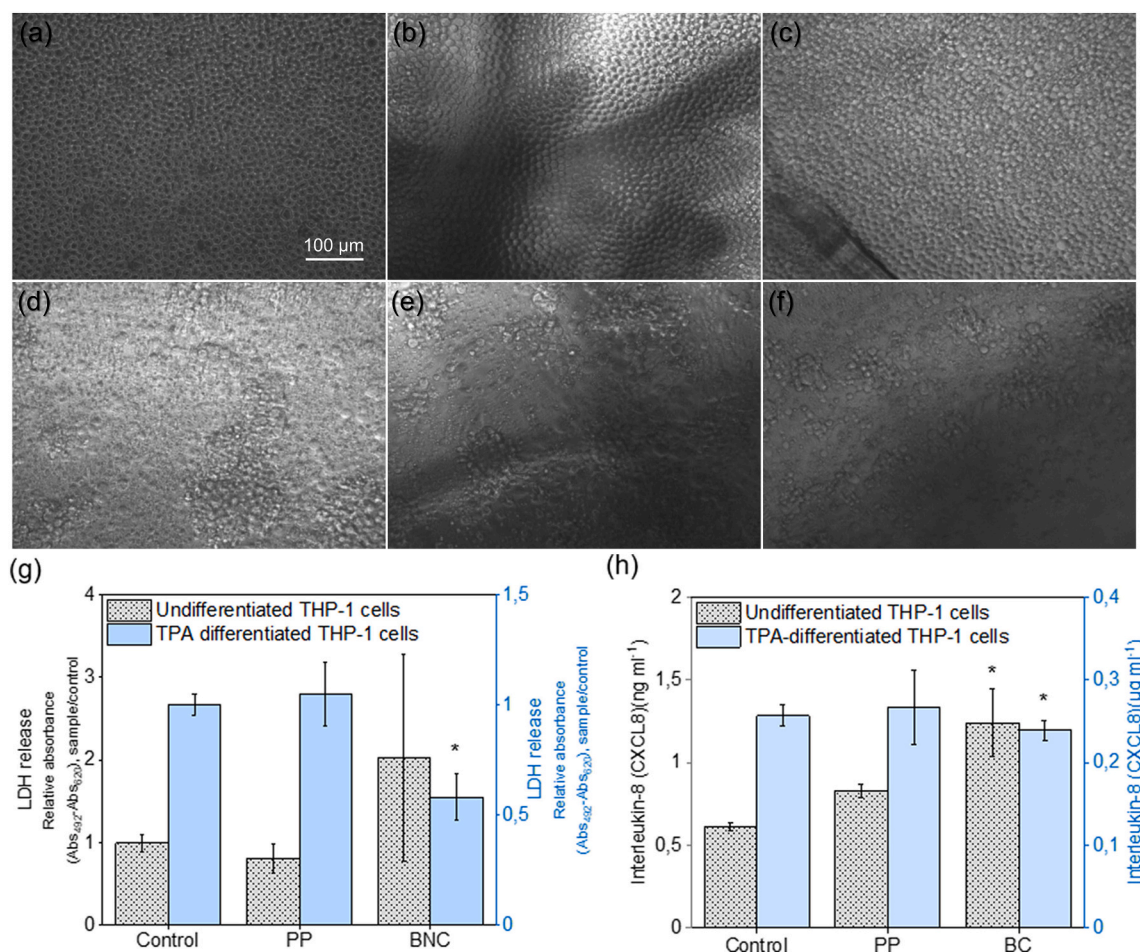

Fig. 6. (a–c) The digital phase-contrast microscopy images ($20\times$ objective) from cultures of THP-1 cells without TPA stimulation. (a) Control without material, (b) polypropylene (PP) mesh, (c) BNC. (d–f) Digital phase-contrast microscopy images ($20\times$ objective) from cultures of TPA (300 nM)-differentiated THP-1 macrophages. (d) Control without material, (e) polypropylene (PP) mesh, (f) BNC. The scale bar from a to f is 100 μm. (g) Lactate dehydrogenase (LDH)-release from cells to culture medium after 3-day incubation of THP-1 cells with the materials, without other external cell stimulation, and with TPA (300 nM)-differentiated THP-1 macrophages (*$p < 0.01$ as compared to Control). (h) Concentrations of interleukin-8 (CXCL8) in culture media after a 3-day incubation of THP-1 cells with the materials, without other external cell stimulation, and with TPA (300 nM)-differentiated THP-1 macrophages (*$p < 0.05$ as compared to Control).

mechanistic understanding of its ability to suppress the TPA-induced pro-inflammatory macrophage-like phenotype as observed here by a decreased secretion of IL-8 after exposure to the BNC.

4. Conclusion

Bacterial nanocellulose outperforms many commonly used thermoplastics in biomedicine due to its similarity to the Extra Cellular Matrix, outstanding mechanical performance in wet conditions, ease of suturing and sterilization, high porosity (mesoporous, macroporous and macroscopic voids), and large surface area. To advance the realm of applications of BNC in biomedical devices, herein, all-nanocellulose BNC meshes with negative Poisson's ratio were produced by following a hybrid manufacturing protocol. Three auxetic cell units, namely, triangle-, round-, and star-shaped were examined to develop structures with overall infill density of 70 ± 3.1% (about 30% openings), 59 ± 2.1, and 62 ± 2.6%, respectively. Depending on the culture time, BNC exhibited tensile strengths of 48–456 MPa (7 to 14 days of incubation), with over 87% stability after 100 burst load/unload cycles at 3% strain. The developed BNC meshes exhibited a negative Poisson's ratio (v = −0.36 to −0.13) *via* hybrid manufacturing. The reversible structural expansion under tension minimizes the tissue damage that commonly occurs by shrinkage of plastic-based mesh implants. Furthermore, the cytotoxicity and interleukin-8 release from THP-1 cells in interaction with BNC was investigated, and it is concluded that BNC drove monocyte activation but suppressed the TPA-induced pro-inflammatory macrophage-like phenotype. The approach presented herein indicates a green method of producing biomaterials for *in-vivo* applications, which are expected to maximize comfort, minimize material fatigue, and thus improve the overall success of future long-term mesh implants. Furthermore, given the range of research streams on bacterial cellulose, where new functionalities can be incorporated, one can expect additional bioactive molecules to be incorporated into such designs, for instance, to facilitate growth or to decrease the risks of infection post-implantation.

The supporting information includes 8 figures. Fig. S1: Setup used to prevent wet BNC structures from slippage during bursting strength tests. Fig. S2: The tensile mechanical tests for wet BNC. Fig. S3: The positive PLA and negative silicon molds with no tilt angle. Fig. S4: Illustration of the challenge of BNC removal from the molds with no tilt angle. Fig. S5: The structure opening, structure infill, and the infill density of the BNC, and the tilt angle in the silicon molds. Fig. S6: The structural development by mold guiding. Fig. S7: Auxetic BNC meshes obtained after culturing for 10 days. Fig. S8: The wet and air-dried BNC structures. Fig. S9: Nitrogen adsorption isotherms. Fig. S10. Polypropylene knitted mesh and the SEM images at 40×, 200×, 1000×, and 15,000×. Fig. S11: The weight loss of BNC in pH 7.4 and pH 5 for 28 days. Supplementary data to this article can be found online at doi:https://doi.org/10.1016/j.carbpol.2022.119198.

CRediT authorship contribution statement

Rubina Ajdary: Conceptualization, Methodology, Formal analysis, Investigation, Writing – original draft, Writing – review & editing, Visualization. **Roozbeh Abidnejad:** Methodology, Investigation, Writing – review & editing, Visualization. **Janika Lehtonen:** Methodology, Investigation, Writing – review & editing, Visualization. **Jani Kuula:** Methodology, Investigation, Writing – review & editing, Visualization. **Eija Raussi-Lehto:** Methodology, Investigation, Writing – review & editing, Visualization. **Esko Kankuri:** Methodology, Formal analysis, Investigation, Writing – original draft, Writing – review & editing, Visualization. **Blaise Tardy:** Methodology, Investigation, Writing – review & editing, Visualization. **Orlando J. Rojas:** Supervision, Funding acquisition, Conceptualization, Writing – review & editing.

Declaration of competing interest

None.

Acknowledgements

References

Ajdary, R., Ezazi, N. Z., Correia, A., Kemell, M., Huan, S., Ruskoaho, H. J., Hirvonen, J., Santos, H. A., & Rojas, O. J. (2020). Multifunctional 3D-printed patches for long-term drug release therapies after myocardial infarction. *Advanced Functional Materials, 30*(34), 1–10. https://doi.org/10.1002/adfm.202003440

Ajdary, R., Reyes, G., Kuula, J., Raussi-Lehto, E., Mikkola, T. S., Kankuri, E., & Rojas, O. J. (2021). Direct ink writing of biocompatible nanocellulose and chitosan hydrogels for implant mesh matrices. *ACS Polymers Au.* https://doi.org/10.1021/acspolymersau.1c00045

Ajdary, R., Tardy, B. L., Mattos, B. D., Bai, L., & Rojas, O. J. (2020). Plant nanomaterials and inspiration from nature: Water interactions and hierarchically structured hydrogels. *Advanced Materials, 2001085.* https://doi.org/10.1002/adma.202001085

Amorim, J. D. P., de Souza, K. C., Duarte, C. R., da Silva Duarte, I., de Assis Sales Ribeiro, F., Silva, G. S., de Farias, P. M. A., Stingl, A., Costa, A. F. S., Vinhas, G. M., & Sarubbo, L. A. (2020). Plant and bacterial nanocellulose: Production, properties and applications in medicine, food, cosmetics, electronics and engineering. A review. *Environmental Chemistry Letters, 18*(3), 851–869. https://doi.org/10.1007/s10311-020-00989-9

Aramwit, P., & Bang, N. (2014). In *The characteristics of bacterial nanocellulose gel releasing silk sericin for facial treatment* (pp. 1–11).

Bao, L., Tang, J., Hong, F. F., Lu, X., & Chen, L. (2020). Physicochemical properties and in vitro biocompatibility of three bacterial nanocellulose conduits for blood vessel applications. *Carbohydrate Polymers, 239*(March), Article 116246. https://doi.org/10.1016/j.carbpol.2020.116246

Barfod, K. W. (2014). Achilles tendon rupture; assessment of nonoperative treatment. *Danish Medical Journal, 61*(4), Article B4837.

Barnes, J. M., Przybyla, L., & Weaver, V. M. (2017). Tissue mechanics regulate brain development, homeostasis and disease. *Journal of Cell Science, 130*, 71–82. https://doi.org/10.1242/jcs.191742

Baylón, K., Rodríguez-Camarillo, P., Elías-Zúñiga, A., Díaz-Elizondo, J. A., Gilkerson, R., & Lozano, K. (2017). Past, present and future of surgical meshes: A review. *Membranes, 7*(3), 1–23. https://doi.org/10.3390/membranes7030047

Bottan, S., Robotti, F., Jayathissa, P., Hegglin, A., Bahamonde, N., Heredia-Guerrero, J. A., Bayer, I. S., Scarpellini, A., Merker, H., Lindenblatt, N., Poulikakos, D., & Ferrari, A. (2015). Surface-structured bacterial cellulose with guided assembly-based biolithography (GAB). *ACS Nano, 9*(1), 206–219. https://doi.org/10.1021/nn5036125

Bungay, H. R., & Serafica, G. C. (1986). *Production of microbial cellulose (Patent No. 6071727)*.

Cai, Q., Hu, C., Yang, N., Wang, Q., Wang, J., Pan, H., Hu, Y., & Ruan, C. (2018). Enhanced activity and stability of industrial lipases immobilized onto spherelike bacterial cellulose. *International Journal of Biological Macromolecules, 109*, 1174–1181. https://doi.org/10.1016/j.ijbiomac.2017.11.100

Cañas-Gutiérrez, A., Martinez-Correa, E., Suárez-Avendaño, D., Arboleda-Toro, D., & Castro-Herazo, C. (2020). Influence of bacterial nanocellulose surface modification on calcium phosphates precipitation for bone tissue engineering. *Cellulose, 27*(18), 10747–10763. https://doi.org/10.1007/s10570-020-03470-6

Castro, C., Cleenwerck, I., Trček, J., Zuluaga, R., de Vos, P., Caro, G., Aguirre, R., Putaux, J. L., & Gañán, P. (2013). Gluconacetobacter medellinensis sp. nov., cellulose- and non-cellulose-producing acetic acid bacteria isolated from vinegar. *International Journal of Systematic and Evolutionary Microbiology, 63*(PART3), 1119–1125. https://doi.org/10.1099/ijs.0.043414-0

Cheng, Q., Liu, Y., Lyu, J., Lu, Q., Zhang, X., & Song, W. (2020). 3D printing-directed auxetic kevlar aerogel architectures with multiple functionalization options. *Journal of Materials Chemistry A, 8*(28), 1423–14253. https://doi.org/10.1039/d0ta02590a

Dällenbach, P. (2015). To mesh or not to mesh: A review of pelvic organ reconstructive surgery. *International Journal of Women's Health, 7*, 331–343. https://doi.org/10.2147/IJWH.S71236

Den Hollander, B., Sundström, M., Pelander, A., Siltanen, A., Ojanperä, I., Mervaala, E., Korpi, E. R., & Kankuri, E. (2015). Mitochondrial respiratory dysfunction due to the conversion of substituted cathinones to methylbenzamides in SH-SY5Y cells. *Scientific Reports, 5*(5), 14294. https://doi.org/10.1038/srep14924

Fallingborg, J. (1999). Intraluminal pH of the human gastrointestinal tract. *Danish Medical Bulletin, 43*(6), 183–196.

Fey, C., Betz, J., Rosenbaum, C., Kralisch, D., Vielreicher, M., Friedrich, O., Metzger, M., & Zdzieblo, D. (2020). Bacterial nanocellulose as novel carrier for intestinal epithelial cells in drug delivery studies. *Materials Science and Engineering C, 109*, Article 110613. https://doi.org/10.1016/j.msec.2019.110613 (December 2019).

Fonseca, D. F. S., Vilela, C., Pinto, R. J. B., Bastos, V., Oliveira, H., Catarino, J., Faísca, P., Rosado, C., Silvestre, A. J. D., & Freire, C. S. R. (2021). Bacterial nanocellulose-hyaluronic acid microneedle patches for skin applications: In vitro and in vivo evaluation. *Materials Science and Engineering C, 118*, Article 111350. https://doi.org/10.1016/j.msec.2020.111350 (March 2020).

Geisel, N., Clasohm, J., Shi, X., Lamboni, L., Yang, J., Mattern, K., Yang, G., Schäfer, K. H., & Saumer, M. (2016). Microstructured multilevel bacterial cellulose allows the guided growth of neural stem cells. *Small, 12*(39), 5407–5413. https://doi.org/10.1002/smll.201601679

Gorgieva, S., & Trček, J. (2019). Bacterial cellulose: Production, modification and perspectives in biomedical applications. *Nanomaterials, 9*(10), 1–20. https://doi.org/10.3390/nano9101352

Greca, L. G., Lehtonen, J., Tardy, B. L., Guo, J., & Rojas, O. J. (2018). Biofabrication of multifunctional nanocellulosic 3D structures: A facile and customizable route. *Materials Horizons, 5*(3), 408–415. https://doi.org/10.1039/c7mh01139c

Greca, L. G., Rafiee, M., Karakoç, A., Lehtonen, J., Mattos, B. D., Tardy, B. L., & Rojas, O. J. (2020). Guiding bacterial activity for biofabrication of complex materials via controlled wetting of superhydrophobic surfaces. *ACS Nano, 14*(10), 12929–12937. https://doi.org/10.1021/acsnano.0c03999

Helenius, G., Bäckdahl, H., Bodin, A., Nannmark, U., Gatenholm, P., & Risberg, B. (2006). In vivo biocompatibility of bacterial cellulose. *Journal of Biomedical Materials Research - Part A, 76A*(2), 431–438. https://doi.org/10.1002/jbm.a.30570

Hong, F., Wei, B., & Chen, L. (2015). Preliminary study on biosynthesis of bacterial nanocellulose tubes in a novel double-silicone-tube bioreactor for potential vascular prosthesis. *BioMed Research International, 560365*. https://doi.org/10.1155/2015/560365

Iakovlev, V. V., Guelcher, S. A., & Bendavid, R. (2015). Degradation of polypropylene in vivo: A microscopic analysis of meshes explanted from patients. *Journal of Biomedical Materials Research - Part B Applied Biomaterials, 105B*(2), 237–248. https://doi.org/10.1002/jbm.b.33502

Jiang, Y., & Li, Y. (2018). 3D printed auxetic mechanical metamaterial with chiral cells and re-entrant cores. *Scientific Reports, 8*, 2397. https://doi.org/10.1038/s41598-018-20795-2

Knight, K. M., Moalli, P. A., & Abramowitch, S. D. (2018). Preventing mesh pore collapse by designing mesh pores with auxetic geometries: A comprehensive evaluation via computational modeling. *Journal of Biomechanical Engineering, 140*(5), 1–8. https://doi.org/10.1115/1.4039058

Lai, C. W., & Yu, S. S. (2020). 3D printable strain sensors from deep eutectic solvents and cellulose nanocrystals. *ACS Applied Materials and Interfaces, 12*(30), 34235–34244. https://doi.org/10.1021/acsami.0c11152

Lakes, R. (1987). Foam structures with a negative poisson's ratio. *Science, 235*, 1038–1040. https://doi.org/10.1126/science.235.4792.1038

Lakes, R. S. (2017). Negative-Poisson's-ratio materials: Auxetic solids. *Annual Review of Materials Research, 47*, 63–81. https://doi.org/10.1146/annurev-matsci-070616-124118

Lee, S. E., & Park, Y. S. (2017). The role of bacterial cellulose in artificial blood vessels. *Molecular and Cellular Toxicology, 13*(3), 257–261. https://doi.org/10.1007/s13273-017-0028-3

Lehtonen, J., Chen, X., Beaumont, M., Hassinen, J., Orelma, H., Dumée, L. F., Tardy, B. L., & Rojas, O. J. (2021). Impact of incubation conditions and post-treatment on the properties of bacterial cellulose membranes for pressure-driven filtration. *Carbohydrate Polymers, 251*(January), Article 117073. https://doi.org/10.1016/j.carbpol.2020.117073

Lin, N., & Dufresne, A. (2014). Nanocellulose in biomedicine: Current status and future prospect. *European Polymer Journal, 59*(October), 302–325. https://doi.org/10.1016/j.eurpolymj.2014.07.025

Liu, Y., & Hu, H. (2010). A review on auxetic structures and polymeric materials. *Scientific Research and Essays, 5*, 1052–1063.

McKenna, B. A., Mikkelsen, D., Wehr, J. B., Gidley, M. J., & Menzies, N. W. (2009). Mechanical and structural properties of native and alkali-treated bacterial cellulose produced by gluconacetobacter xylinus strain ATCC 53524. *Cellulose, 16*(6), 1047–1055. https://doi.org/10.1007/s10570-009-9340-y

Naomi, R., Idrus, R. B. H., & Fauzi, M. B. (2020). Plant-vs. bacterial-derived cellulose for wound healing: A review. *International Journal of Environmental Research and Public Health, 17*(18), 1–25. https://doi.org/10.3390/ijerph17186803

Oliveira Barud, H. G., da Silva, R. R., Borges, M. A. C., Castro, G. R., Ribeiro, S. J. L., & da Silva Barud, H. (2020). Bacterial nanocellulose in dentistry: Perspectives and challenges. *Molecules (Basel, Switzerland), 26*(1). https://doi.org/10.3390/molecules26010049

Pang, M., Huang, Y., Meng, F., Zhuang, Y., Liu, H., Du, M., Ma, Q., Wang, Q., Chen, Z., Chen, L., Cai, T., & Cai, Y. (2020). Application of bacterial cellulose in skin and bone tissue engineering. *European Polymer Journal, 122*, Article 109365. https://doi.org/10.1016/j.eurpolymj.2019.109365 (July 2019).

Papadopoulou, A., Laucks, J., & Tibbits, S. (2017). Auxetic materials in design and architecture. *Nature Reviews Materials, 2*, 1–3. https://doi.org/10.1038/natrevmats.2017.78

Prawoto, Y. (2012). Seeing auxetic materials from the mechanics point of view: A structural review on the negative Poisson's ratio. *Computational Materials Science, 58*, 140–153. https://doi.org/10.1016/j.commatsci.2012.02.012 (June 2012).

Queirós, E. C., Pinheiro, S. P., Pereira, J. E., Prada, J., Pires, I., Dourado, F., Parpot, P., & Gama, M. (2021). Hemostatic dressings made of oxidized bacterial nanocellulose membranes. *Polysaccharides, 2*(1), 80–99. https://doi.org/10.3390/polysaccharides2010006

Ross, P., Mayer, R., & Benziman, M. (1991). Cellulose biosynthesis and function in bacteria. *Microbiological Reviews, 55*(1), 35–58.

Rueden, C. T., Schindelin, J., Hiner, M. C., DeZonia, B. E., Walter, A. E., Arena, E. T., & Eliceiri, K. W. (2017). Image J2: ImageJ for the next generation of scientific image data. *Microscopy and Microanalysis, 18*(1), 529. https://doi.org/10.1186/s12859-017-1934-z

Rühs, P. A., Malollari, K. G., Binelli, M. R., Crockett, R., Balkenende, D. W. R., Studart, A. R., & Messersmith, P. B. (2020). Conformal bacterial cellulose coatings as lubricious surfaces. *ACS Nano, 14*(4), 3885–3895. https://doi.org/10.1021/acsnano.9b09956

Savchenko, M. (2021). Normal vaginal pH: How to test, balance, and restore vaginal pH. https://flo.health/menstrual-cycle/health/symptoms-and-diseases/normal-vaginal-ph-balance.

Stavric, M., & Wiltsche, A. (2019). Geometrical elaboration of auxetic structures. *Nexus Network Journal, 21*(1), 79–90. https://doi.org/10.1007/s00004-019-00428-5

Sternschuss, G., Ostergard, D., & Patel, H. (2012). Post-implantation alterations of polypropylene in the human. *The Journal of Urology, 188*(1), 27–31. https://doi.org/10.1016/j.juro.2012.02.2559

Tang, W., Jia, S., Jia, Y., & Yang, H. (2010). The influence of fermentation conditions and post-treatment methods on porosity of bacterial cellulose membrane. *World Journal of Microbiology and Biotechnology, 26*(1), 125–131. https://doi.org/10.1007/s11274-009-0151-y

U.S. Food, & Drug Administration. (2021). FDA takes action to protect women's health, orders manufacturers of surgical mesh intended for transvaginal repair of pelvic organ prolapse to stop selling all devices accessed July https://www.fda.gov/news-events/press-announcements/fda-takes-action-protect-womens-health-orders-manufacturers-surgical-mesh-intended-transvaginal.

Väänänen, A. J., Salmenperä, P., Hukkanen, M., Rauhala, P., & Kankuri, E. (2006). Cathepsin B is a differentiation-resistant target for nitroxyl (HNO) in THP-1 monocyte/macrophages. *Free Radical Biology and Medicine, 41*(1), 120–131. https://doi.org/10.1016/j.freeradbiomed.2006.03.016

Verma, P., Shofner, M. L., & Griffin, A. C. (2014). Deconstructing the auxetic behavior of paper. *Physica Status Solidi (B) Basic Research, 251*(2), 289–296. https://doi.org/10.1002/pssb.201384243

Wang, J., Tavakoli, J., & Tang, Y. (2019). Bacterial cellulose production, properties and applications with different culture methods – A review. *Carbohydrate Polymers, 219* (May), 63–76. https://doi.org/10.1016/j.carbpol.2019.05.008

Wang, S., Li, T., Chen, C., Kong, W., Zhu, S., Dai, J., Diaz, A. J., Hitz, E., Solares, S. D., Li, T., & Hu, L. (2018). Transparent, anisotropic biofilm with aligned bacterial cellulose nanofibers. *Advanced Functional Materials, 28*(24), 1707491. https://doi.org/10.1002/adfm.201707491

Xu, T., Jiang, Q., Ghim, D., Liu, K. K., Sun, H., Derami, H. G., Wang, Z., Tadepalli, S., Jun, Y. S., Zhang, Q., & Singamaneni, S. (2018). Catalytically active bacterial nanocellulose-based ultrafiltration membrane. *Small, 14*(15), 1–8. https://doi.org/10.1002/smll.201704006

Yang, J., Wang, L., Zhang, W., Sun, Z., Li, Y., Yang, M., Zeng, D., Peng, B., Zheng, W., Jiang, X., & Yang, G. (2018). Reverse reconstruction and bioprinting of bacterial cellulose-based functional total intervertebral disc for therapeutic implantation. *Small, 14*(7), Article 1702582. https://doi.org/10.1002/smll.201702582

Yao, Y. T., Alderson, K. L., & Alderson, A. (2016). Modeling of negative Poisson's ratio (auxetic) crystallie cellulose. *Cellulose, 23*, 3429–3448. https://doi.org/10.1007/s10570-016-1069-9

Yuan, H., Chen, L., Hong, F. F., & Zhu, M. (2018). Evaluation of nanocellulose carriers produced by four different bacterial strains for laccase immobilization. *Carbohydrate Polymers, 196*(May), 457–464. https://doi.org/10.1016/j.carbpol.2018.05.055